

Thomas S. Hug · Nicolas F. de. Rooij · U. Stauffer

Fabrication and electroosmotic flow measurements in micro- and nanofluidic channels

Received: 29 October 2004 / Accepted: 14 June 2005 / Published online: 31 July 2005
© Springer-Verlag 2005

Abstract An easy method for fabricating micro- and nanofluidic channels, entirely made of a thermally grown silicon dioxide is presented. The nanochannels are up to 1-mm long and have widths and heights down to 200 nm, whereas the microfluidic channels are 20- μm wide and 4.8- μm high. The nanochannels are created at the interface of two silicon wafers. Their fabrication is based on the expansion of growing silicon dioxide and the corresponding reduction in channel cross-section. The embedded silicon dioxide channels were released and are partially freestanding. The transparent and hydrophilic silicon dioxide channel system could be spontaneously filled with aqueous, fluorescent solution. The electrical resistances of the micro- and nanofluidic channel segments were calculated and the found values were confirmed by current measurements. Electrical field strengths up to 600 V/cm were reached within the nanochannels when applying a potential of only 10 V. Electroosmotic flow (EOF) measurements through micro- and nanofluidic channel systems resulted in electroosmotic mobilities in the same order of those encountered in regular, fused silica capillaries.

Keywords Micro- and nanofluidic channels · Electroosmotic flow

1 Introduction

Microfluidic devices have wide applications in handling liquids in biology and chemistry for manipulating samples for fast, high resolution, low-cost analysis and synthesis. Reducing the cross-section of microfluidic channels down to the nanometer scale is attractive for

detecting, transporting, manipulating and sorting single molecules such as DNA (Foquet et al. 2003, 2004; Turner et al. 1998). Microfluidic interfaces to nanosized pores, pillars or channels have proven to be useful to separate and fractionate DNA (Cabodi et al. 2002; Cao et al. 2002a, b; Chou et al. 1999; Baba et al. 2003). Having a stretched DNA molecule in a nanochannel presents an attractive perspective for linear analysis of DNA (Tegenfeldt et al. 2002, 2004). Reducing the channel height down to the double layer thickness on the order of 10 nm is attractive to locally enriched ions (Pu et al. 2004). Other applications of micro- and nanofluidic channel systems include nanometer-sized injection channels resulting in lower injection volumes and reduced backflow (Zhang and Manz 2001; Kuo et al. 2003a, b).

The selection of the material and the technique for fabricating the nanochannels is guided by concerns about the channel filling by capillary effects. Filling by capillary forces, electroosmotic flow (EOF) and an increased surface to volume ratio are major concerns, which influence the choice of suitable materials for nanochannels and its fabrication technique (Tas et al. 2003). Sacrificial layer etching, nanoimprint lithography, e-beam lithography and other methods have already been successfully applied for nanochannel fabrication (Guo et al. 2004; Yu et al. 2003; Cao et al. 2002a, b; Hibara et al. 2002; Lee et al. 2003; O'Brien et al. 2003). Nanochannels were fabricated in glass, silicon, polyimide, PDMS and Au (Eijkel et al. 2004; Hug et al. 2003; Zaumseil et al. 2003).

The miniaturization of microfluidic electrophoretic separations in a single nanochannel seems especially attractive since it results in smaller samples volumes, shorter column lengths and separation times. With a potential of 10 V across a 100- μm -long channel, the field strength of 1 kV/cm is reached, a value typically used in capillary electrophoresis. While the miniaturization of centimetre-long microfluidic channels down to micrometre-short nanochannels is straightforward, the corresponding reduction of the reservoirs is limited in practice

T. S. Hug (✉) · N. F. de. Rooij · U. Stauffer
Institute of Microtechnology, University of Neuchâtel,
Rue Jaquet-Droz 1, 2007 Neuchâtel, Switzerland
E-mail: thomassilvan@bluemail.ch
Tel.: +41-78-66255561
Fax: +41-1-9107466

by evaporation. To keep the necessary field strength in the nanochannel region, liquid reservoirs and nanochannels must thus be connected by microfluidic channels with a low electrical resistance. Our aim was to develop simple fabrication methods for micro- and nanofluidic channel systems suitable for electrophoretic separation. By combining microfluidic access channels with nanochannels and a 10 V source, field strengths up to 600 V/cm were achieved.

2 Experimental

2.1 Fabrication

The micro- and nanofluidic system features the following basic elements: inlet holes, which also serve as reservoirs, microfluidic access channels and the proper nanochannels. The fabrication of this system is based on photolithography, Si-etching, fusion bonding and thermal oxidation. It is shown in Fig. 1. The first, top wafer is a 390- μm thick, double-side-polished silicon (100) wafer (Siltronix, Geneva, Switzerland). The future channel system is outlined on this wafer and etched into its surface. The second, bottom wafer has the same orientation as the top wafer and features the inlet holes which were KOH-etched through-holes with a dimension of $20 \times 20 \mu\text{m}^2$ at the bottom side. The groove system in the top wafer was fabricated in two steps: first, the future nanochannels are defined by photolithography and deep reactive ion etching (DRIE). These grooves were initially 1.5- μm deep, 1.5 and 4.5- μm wide and either 100, 300 or 1,000- μm long. The layout was either straight or in a meander form. After etching, the wafers were cleaned and oxidized in order to protect the grooves. A second lithography step was then used to delineate the access channels to the nanochannels. This pattern was transferred by means of buffered BHF into the oxide, which was then used as an etch mask for KOH etching of the 5- μm -deep grooves for the future access channels. These grooves had a width of 20.5 μm at the top. Due to the overlap of the two lithographies and the KOH etching the length of the future nanochannels was reduced by 20 μm . A picture of the top wafer after these processing steps is shown in Fig. 2a. Both, top and bottom wafer were then cleaned and aligned such that the inlet-holes meet the end of an access groove (Fig. 1b). After alignment, the two wafers were fused together in a wet-oxidizing atmosphere at 1,100°C. During this step, a 1- μm -thick oxide was grown also inside the channel system, which was open to the oxidizing atmosphere via the inlet-holes. This reduced the cross-section of the channels into the nanometer region (Fig. 2c, d). In the next step, the oxide of the top wafer was structured by photolithography and reactive ion etching (RIE) such that a window could be etched into the silicon by KOH, providing optical access to the transparent nanochannels (Fig. 1c). Continuous etching

in KOH finally released the nanochannels completely. About 400 linear nanochannels with microfluidic access channels could be manufactured per wafer pair. This number is primarily limited by the size of the inlet-holes.

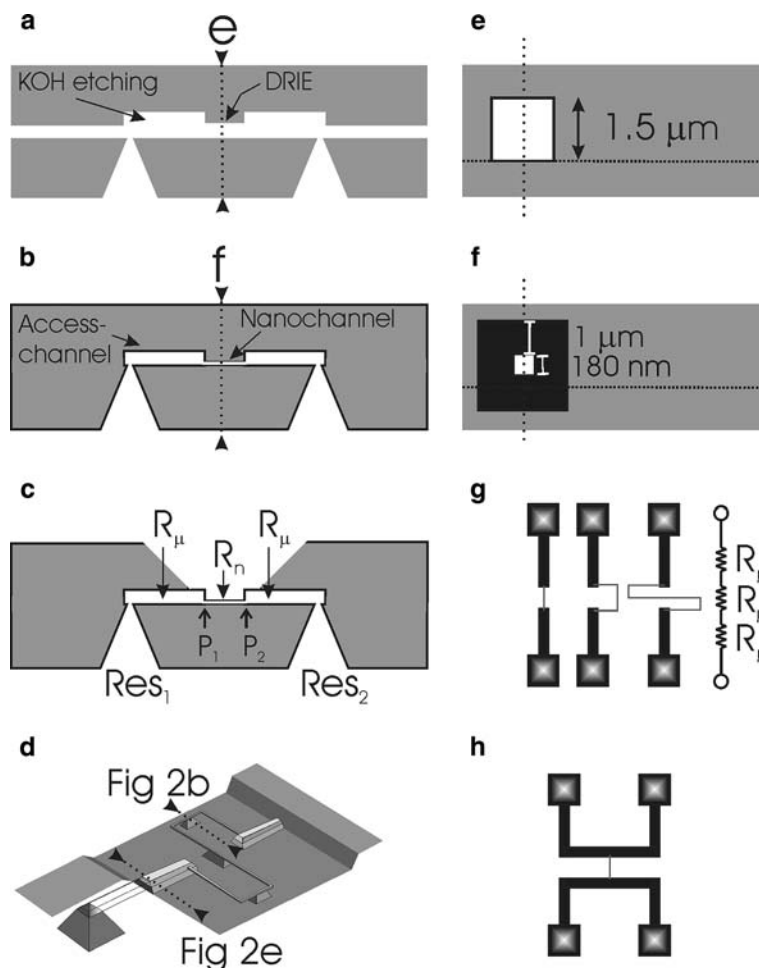
2.2 Filling of micro- and nanofluidic channel system

As shown in Fig. 2f, the complete fluidic system was filled with a solution containing 0.1 M NaCl, 0.01 M $\text{NaH}_2\text{PO}_4/\text{Na}_2\text{HPO}_4$ buffer (pH 7) and 1 mM fluorescein. The fluorescein was employed to visualize the filling process. In the case of the 3.5- μm wide and 600-nm-high nanochannel, the filling of the complete capillary system was spontaneous due to capillary forces. In the case of the 200-nm-wide nanochannels, the dosing of liquid to the first reservoir (Res₁, Fig. 1c) resulted in spontaneous filling of the first microfluidic access channels as well as the nanochannels (P_2 , Fig. 1c). The second microfluidic channel, however, did not spontaneously fill, probably for the following possible reasons: either the shape of the transition between the nanochannel and the microchannel section represents a capillary stop or the flow through the nanocapillary driven by the capillary forces of the microchannel becomes so slow that evaporation is dominant. According to the law of Poiseuille, the flow F driven by the pressure drop Δp increases with the fourth power of the radius r of the tube with length l

$$F = \frac{\Delta p \times \pi \times r^4}{8 \times \eta \times l} \quad (1)$$

where η is the hydrodynamic viscosity. Reducing the nanochannel diameter by one order of magnitude requires up to 10^4 more time for the filling of the second microfluidic channel via the nanochannel, which may become beyond any reasonable observation time. The alternative approach of filling the system from both ends resulted in a filled channel system with enclosed air bubbles. There is thus a certain limit of nanochannel dimension beyond, which more than two microfluidic access channels and reservoirs per nanochannel are needed in order to assure filling by capillary forces as shown in Fig. 1h. In the micro- and nanofluidic channel system of Fig. 1h, one microfluidic channel, say the top one, is first filled either by capillary forces or by pressure from left to right. The filling of the first microfluidic access channel will spontaneously induce also the filling of the nanofluidic channel by capillary forces. Then, the second microfluidic channel, say the bottom one in Fig. 1h, is also filled from left to right. By this, the air will not be trapped at the interface between the nanofluidic channel and the second microfluidic channel but vented through the bottom right reservoir. Besides filling, the fluidic scheme of Fig. 1h gives also more freedom for EOF measurements. By filling the microfluidic access channels with two solutions having a different conductivity, EOF measurements through only the nanochannel section become possible.

Fig. 1 Fabrication scheme: **a** *Top wafer* with the microfluidic channel system and *bottom wafer* with inlet holes were carefully aligned. **b** During a wet oxidation a homogeneous silicon dioxide in the order of $1\ \mu\text{m}$ is grown, which reduces the channel dimensions as shown in **e** and **f**. **c** In the next step the silicon dioxide on the backside is photolithographically structured to selectively release the embedded silicon dioxide channels in KOH. **d** Schematic view of the freestanding $980\text{-}\mu\text{m}$ -long silicon dioxide nanochannel standing on three silicon bases. **e** Design layout of the channel system showing the reservoirs, the microfluidic access channels and the 80 , 280 and $980\text{-}\mu\text{m}$ -long nanochannels. A schematic representation of the impedances R_m and R_n of the micro- and nanochannels is given on the right. **f** Filling of micro- and nanofluidic systems by capillary forces require four access channels depending on the nanochannel dimension



2.3 Electroosmotic flow (EOF) measurements

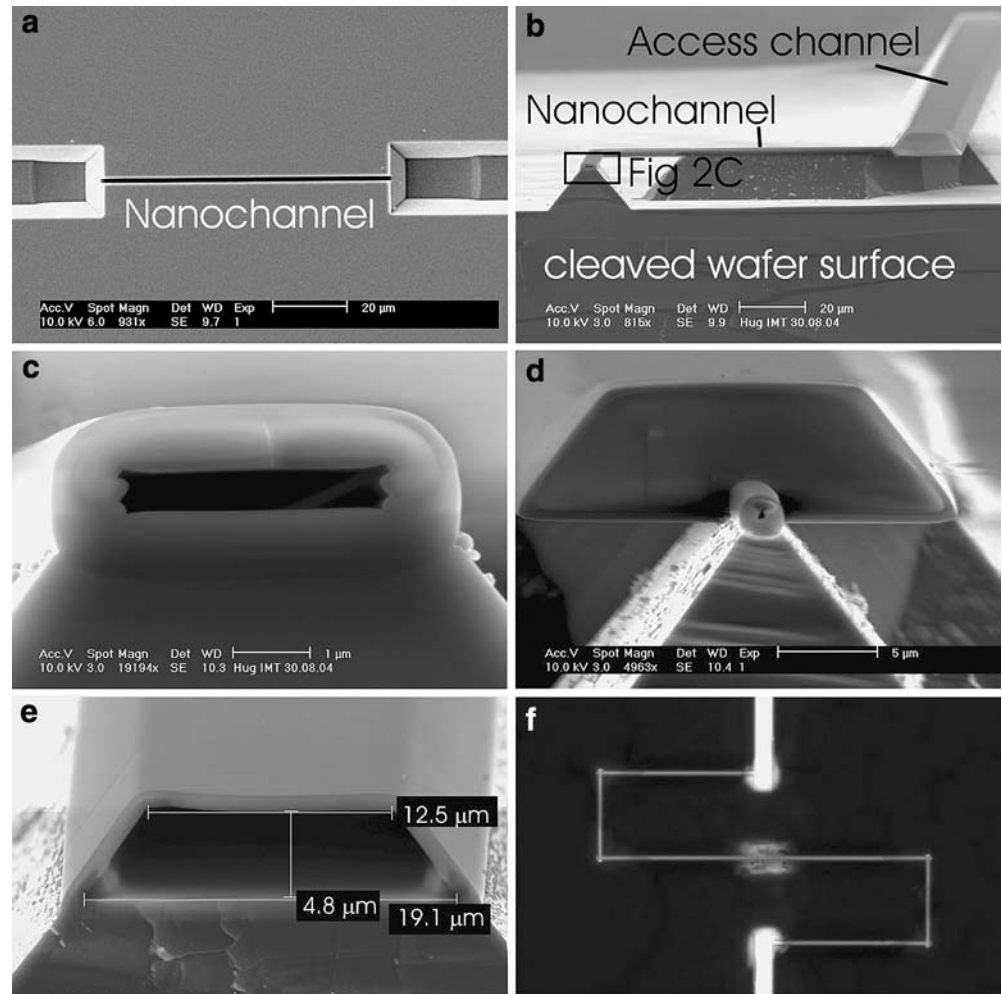
The electroosmotic flow measurements were thus performed with micro- and nanofluidic channel systems consisting of a $3.5\text{-}\mu\text{m}$ wide and 600-nm -high nanochannel connected to two 1.5-mm -long microfluidic access channels with 4.8 and $12.5\text{-}\mu\text{m}$ height respectively, $19.1\text{-}\mu\text{m}$ width as shown in Fig. 2e. Electroosmotic flow measurements were based on current measurements according to the method of Huang et al. 1988. The conductivity measurements were performed with a Labview-controlled Keithley-236-Source-Measure-Unit. To reduce concentration variations due to evaporation, the reservoirs were enlarged by a 3-mm -high poly(dimethylsiloxane) (PDMS, Sylgard 184, Dow Corning, Midland, MI, USA) layer with access holes. The Ag/AgCl electrodes were immersed into both reservoirs. Prior to carrying out conductivity measurements, the channel system was flushed with $0.1\ \text{M}$ NaCl, $0.01\ \text{M}$ $\text{NaH}_2\text{PO}_4/\text{Na}_2\text{HPO}_4$ buffer (pH 7) by means of EOF until the electric current became stable in order to establish a baseline. For the proper EOF-measurements, the reservoir at the cathode side was then replaced with a solution containing $0.02\ \text{M}$ NaCl, $0.01\ \text{M}$ $\text{NaH}_2\text{PO}_4/\text{Na}_2\text{HPO}_4$ buffer (pH 7). Then the driving potential between 5 and $40\ \text{V}$ was applied for a fixed time interval of

$1\text{--}5$ min, inducing EOF. The EOF was then reversed for the same time period by applying a negative potential. As shown in Fig. 4, one EOF-cycle was reproducibly repeated for the same channel three times. For the three different micro- and nanofluidic channel systems, three independent EOF-measurements consisting of three EOF-cycles each were performed. The conductivity of the $10\ \text{mM}$ phosphate buffers containing $0.1\ \text{M}$ NaCl ($\sigma_1 = 12.96\ \text{mS}$, 100%) or $0.02\ \text{M}$ NaCl ($\sigma_2 = 4.84\ \text{mS}$, 37%) was measured with an Orion instrument (Hügli Labortechnik, Switzerland).

3 Results and discussion

The formation of a layer of thermal oxide (100% volume) occurs through the consumption of 44% of silicon (by volume). Accordingly, a $1.5\text{-}\mu\text{m}$ -wide square microchannel results in a 180-nm -wide nanochannel after growing a $1\text{-}\mu\text{m}$ -thick oxide. The formation of silicon dioxide by thermal oxidation is a standard process in thin film technology, and its kinetics was described in a mathematical model by Deal and Grove (1965) and Verdi et al. 1994. Due to the different kinetics of the wet and dry oxidation process, silicon dioxide layers in the order of $1\ \mu\text{m}$ are preferably formed by water vapour

Fig. 2 SEM-characterization and filling: **a** SEM view of the *top wafer* showing the microfluidic access channels and the future nanochannel. **b** View on a cleaved and slightly tilted micro- and nanofluidic channel system showing a nanochannel in the front and microfluidic access channel in the back. Depending on the orientation, the nanochannel became freestanding in the corners. **c** Close-up view of the cross-section of the cleaved nanochannel shown in **b**. **d** A square profile with 1.5- μm length resulted in a 2D-nanochannel with 200-nm inner diameter after the growth of a 1- μm -thick thermal oxide. **e** Close-up view of the microfluidic access channel. **f** A fluorescent microscope was used to observe the filling of the micronanochannels and nanochannels

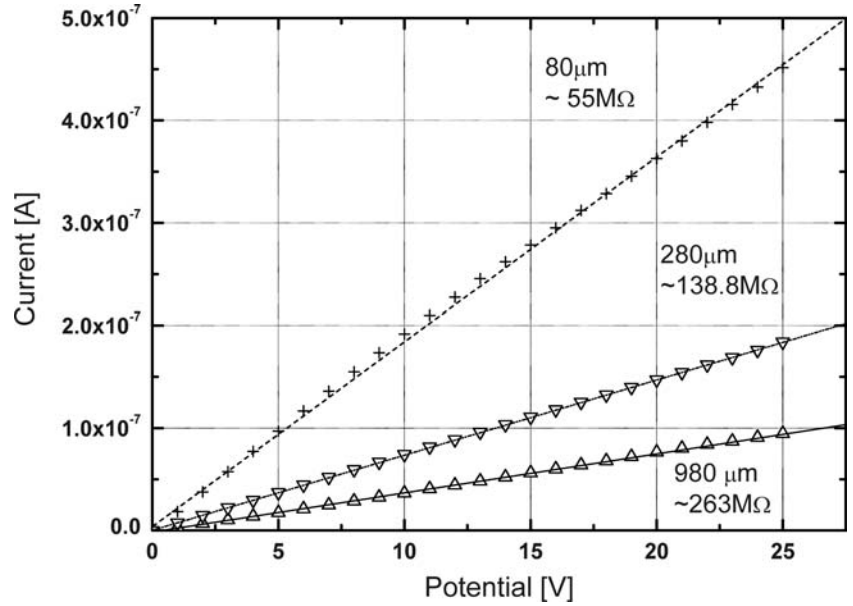


rather than pure oxygen as an oxidizing species. The linear–parabolic model developed by Deal and Grove assumes that the oxidation occurs as a result of two processes that sequentially transport the water vapour through the silicon dioxide layer to the silicon interface, where it is consumed as the silicon dioxide is formed. In the beginning, the growth rate is linear and limited by the chemical reaction at the interface. As the silicon dioxide becomes thicker, the diffusion through the dioxide layer becomes the rate-determining step, which corresponds to the parabolic regime of the model by Deal and Grove. This regime is reached within the order of minutes, depending on the temperature. Growing thick layers of silicon dioxide always takes place in this diffusion-limited regime. The diffusion in the gas phase, on the other hand, is much larger than through the silicon dioxide. Hence, it is this latter that is governing the growth rate also in our fabrication process and this, we believe, is also the reason why the oxide thickness is homogeneous even in millimeter-long channels as found and presented in this study. The homogeneity of the silicon oxide thickness was experimentally confirmed by different designs and by many repetitions. The parallel use of three different widths, namely 1.5, 2.5 and 4.5 μm ,

various nanochannel lengths as well as many other designs (data not shown) were very useful to verify the reproducibility of this process. The silicon oxide thickness was determined from SEM-measurements by either comparing the channel dimensions before and after the thermal oxidation or directly from cleaved channels as shown in Fig. 2b–e. Figure 2b shows a released channel-system with a cleaved nanochannel in the front. During the release step, the silicon dioxide nanocapillaries were underetched in KOH such that they became partly freestanding at rectangular corners. A profile of an originally 4.5- μm wide and 1.8- μm deep rectangular groove resulted in a 3.5- μm wide and 600-nm high, transparent silicon dioxide channel (Fig. 2c). In contrast, an almost square profile with 1.5- μm side length turned into a 200-nm wide round capillary. The profile of the trapezoidal access channels is shown in Fig. 2e.

In a serial sequence of channels the electric field may differ within each channel segment due to differing length or cross-sections. The total resistance R_{tot} of a channel system can be modelled and calculated by treating each channel segment as a resistor R with a resistance proportional to the channel length, L and inversely proportional to the solution's conductivity

Fig. 3 Total channel resistance: from the currents measured between 0 and 25 V the total channel resistance R_{tot} of the channel system with varying nanochannel length L_n was calculated as shown in Table 1



σ and the cross-sectional area of the channel A (Chien and Helmer 1991). In our case, this leads to a total resistance of

$$R_{\text{tot}} = \frac{1}{\sigma} \left[\frac{2\mu}{A_\mu} + \frac{L_n}{A_n} \right], \quad (2)$$

where the indices μ and n refer to the micro- and the nanochannel, respectively.

The electrical resistance as listed in Table 1 were calculated for the 0.1 M NaCl phosphate buffer. The electric field strength E in the micro- and nanochannels were calculated for a potential difference between the reservoirs of 10 V. From the current measurements (cf. Fig. 3) through the channel systems, the total resistances were also experimentally derived. These values are presented in Table 1 as “ R_{tot} (measured)”.

In order to better visualize the different electric field strengths in the individual channel segments, the EOF flow measurements according to Huang were performed with a 37% ($\sigma_2 = 4.84$ mS) instead of a 95% conductivity solution. The experimental data were compared with a model calculation adapted from the one reported by Chien and Helmer (1991) and Chien and Burgi (1992).

The electroosmotic mobility depends on the thickness of the electrical double layer, which is proportional to

the square root of the ionic strength of the electrolyte. The bulk flow (v_b) is then given by the mobility times the electric field strength. In a microfluidic channel containing two sections filled with different buffers of conductivity σ_1 and σ_2 , respectively, v_b can be described by the following equation derived by Chien and Helmer (1991):

$$v_b = \frac{1/\sigma_1 \times x_{\text{eo1}}}{1/\sigma_1 \times x + 1/\sigma_2 \times (1-x)} + \frac{1/\sigma_2 \times (1-x) \times v_{\text{eo2}}}{1/\sigma_1 \times x + 1/\sigma_2 \times (1-x)}, \quad (3)$$

where x is the fraction of the capillary of total length L filled with the first buffer (σ_1), and v_{eo1} and v_{eo2} are the electroosmotic velocities in the channel when completely filled with solution 1 or 2, respectively. Due to mass and charge conservation, the electroosmotic velocity through the nanochannels is inversely proportional to the cross-sections. Based on that, the equivalent length of a microchannel can be computed, which would be passed in the same time t_n as the nanochannel by the front of σ_2 travelling with v_μ : $L_{\text{eq}} = t_n v_\mu = L_n A_n / A_\mu$. Hence, a total equivalent length $L_{\text{eq,tot}}$ of the channel system can be described by $L_{\text{eq,tot}} = 2 \times L_\mu + L_n \times A_n / A_\mu$.

The relation of the electroosmotic velocities $v_{\text{eo1}}/v_{\text{eo2}}$ as a function of ionic strength I was approximated by

Table 1 Overview of resistances R , electrical fields E , electroosmotic velocities v_{EOF} of micro- and nanofluidic channel segments

Nanochannel length (μm)	$2 \times R_\mu$ (M Ω)	R_n (M Ω)	R_{tot} (M Ω)	R_{tot} (measured) (M Ω)	E_μ (V/cm) @ 10 V	E_n (V/cm) @ 10 V	$v_{\text{EOF,n,b}}$ (cm/s) (measured) @ 20 V
80	<i>31.6</i>	<i>29.4</i>	<i>61</i>	55	<i>17.3</i>	<i>602</i>	0.25
280	<i>29.6</i>	<i>103</i>	<i>139.6</i>	138.8	<i>8</i>	<i>277</i>	0.11
980	<i>29.6</i>	<i>367</i>	<i>396.7</i>	263	<i>2.7</i>	<i>94</i>	0.06

Cross-sections of the micro- and nanofluidic channels were 75.8 and 2.1 μm^2 . Calculated values are given in *italics*

their conductivity $v_{eo1}/v_{eo2} \approx (I_2/I_1)^{1/2} \approx (\sigma_2/\sigma_1)^{1/2} = 1.63$ (Thormann et al. 1998).

Based on these two assumptions, the current through the micro and nanofluidic channel system as a function of time shown in Fig. 4 was simulated as follows: the total resistance $R_{tot}(x)$ was calculated as a function of the fraction x of the equivalent capillary length $L_{eq, tot}$ filled with the first buffer (σ_1). The transition of the nanochannel section was not modelled in detail since the front between solutions 1 and 2 passes the nanochannel almost instantaneously in comparison to the time spent in microfluidic channel sections, which were both of identical length, and therefore we obtain:

$$R_{tot}(x) = \frac{2 \times L_\mu \times x}{\sigma_1 \times A_\mu} + \frac{2 \times L_\mu \times (1-x)}{\sigma_2 \times A_\mu} + \frac{L_n}{\sigma_i \times A_n} \Big|_{i=1,2} \begin{cases} 1 & \text{for } x < 0.5 \\ 2 & \text{for } x > 0.5 \end{cases} \quad (4)$$

The bulk velocity (Eq. 3) $v_b(x)$ is equal dx/dt , hence, the time $t(x)$ can be calculated by separation of the variables and numerical integration:

$$t(x) = \int_0^x \frac{d\xi}{v_b(\xi)} \quad (5)$$

From Eq. 4, the current $I(x) = V/R_{tot}(x)$ can be calculated and plotted versus $t(x)$ (Eq. 5). Dashed lines in Fig. 4 shows the modelled values for the electroosmotic velocities $v_{eo1} = 4 \times 10^{-3}$ cm/s, respectively, $v_{eo2} = 6.9 \times 10^{-3}$ cm/s at the electrical field strength $E_\mu = 16$ V/cm.

The model basically illustrates two phenomena. First, the electroosmotic bulk velocity becomes steadily slower as the 10 mM phosphate buffer containing 0.1 M NaCl

is replaced by 0.02 M NaCl and vice versa. In fact the average electroosmotic velocity described by Eq. 3 is not only weighted over the filled lengths of their components but also weighted over their partial conductivities or resistances (Chien and Helmer 1991; Chien and Burgi 1992). Second, the relatively high resistance and the comparatively low volume of the nanochannel results in a characteristic, step-like current drop.

Experimentally, two buffer solutions were sent up to three times through the nanochannel segment by inverting the potential between the electrodes after each passage. In Fig. 4 six consecutive conductivity measurements are compared with a theoretical curve based on the modelled bulk flow and the calculated resistances of the individual channel segments. Both the theoretical and experimental curves nicely illustrate the different electrical field strengths and the different slopes of the current in the individual channel segments. Moreover, the continuous change of the bulk flow due to changing ionic strength of the buffer was confirmed by the experimental data. However, the fast flow of the liquid through the nanometer-sized constrictions, which in our simplified theory should result in a sharp current step, was blurred out for the following possible reasons: first, the pressure difference caused by the mismatch between local electroosmotic velocity and the bulk velocity results in laminar flow and, hence, in broadening of the front between solutions 1 and 2. Second, the geometrical transition of the micro- to the nanochannel region does not represent a perfect funnel and causes mixing and broadens the expected 'current step' in the nanochannel.

From the EOF-measurements the electroosmotic bulk velocity $v_{EOF,b}$ in micro- and nanochannels and the electroosmotic bulk mobility $\mu_b = v_{EOF,n}/E_n$ were calculated (Fig. 5 and Table 2). The calculated mobility in the 80 and 280- μ m-long channel systems differs from the one in a 980- μ m-long channel system due to the higher

Fig. 4 EOF-flow measurement: six consecutive current measurements through a micro- and nanofluidic channel system with a 280- μ m-long, 3.5- μ m wide and 600-nm-high nanochannel at 20 V. Positive currents indicate the electroosmotic flow from 0.02 M NaCl to the 0.1 M NaCl reservoir, whereas negative currents indicate the reversed flow. Dotted lines represent the modelled values based on the calculated channel resistances and the measured conductivities of the buffers

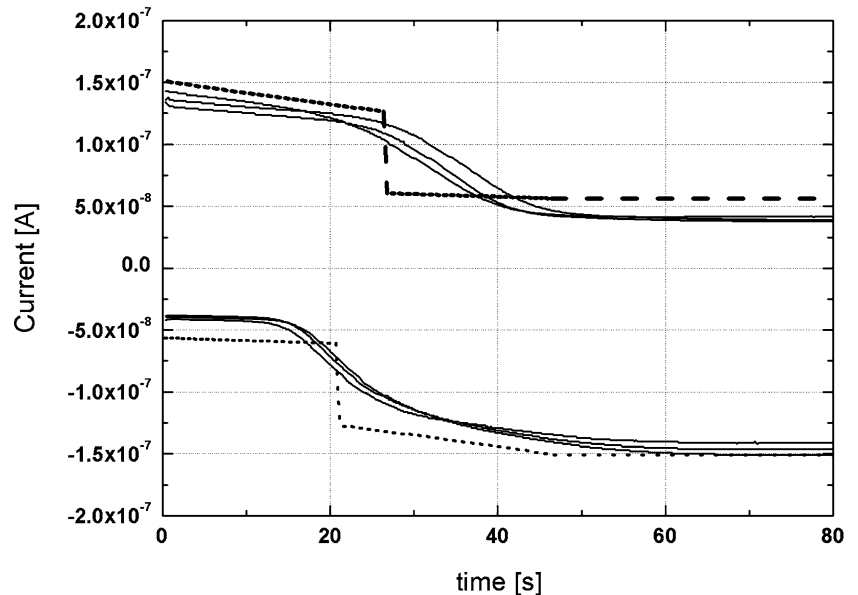
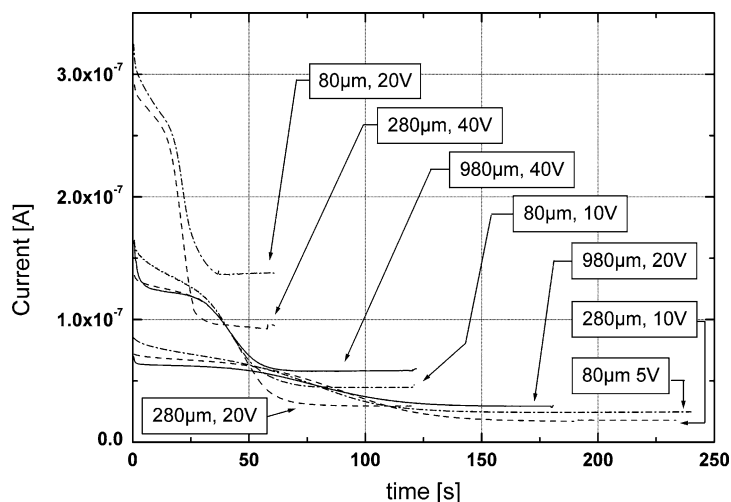


Fig. 5 EOF-flow measurement: overview of each type of current measurement through micro- and nanofluidic channel system with a 80, 280 or 980- μm long, 3.5- μm wide and 600-nm-high nanochannels at 5, 10, 20 or 40 V. Each curve represents the mean of three consecutive measurements



relative error of the experimental versus the theoretical resistance in the 980- μm -long channel system (Table 1). The electroosmotic bulk velocities and mobilities correspond to a 0.06 M NaCl, 10 mM phosphate solution.

The determined electroosmotic mobilities in silicon dioxide micro- and nanofluidic channel system are in the range of the electroosmotic mobilities of fused silica capillaries ($5 \times 10^{-4} \text{ cm}^2/\text{V s}$) and borosilicate glass capillaries ($1.5 \times 10^{-3} \text{ cm}^2/\text{V s}$) under similar conditions (Huang et al. 1988; Gaudioso et al. 2002).

4 Summary and conclusion

A novel fabrication method for micro- and nanofluidic systems was presented. Using only well-established fabrication steps such as standard photolithography, dry and wet etching and thermal oxidation, up to 400 microfluidic–nanofluidic capillaries were fabricated on a single 4-in wafer. This emphasises the potential of the process for large-scale production. Unique is also the realization of a microfluidic–nanofluidic system in pure silicon dioxide having a homogeneous zeta-potential distribution and a minimal peak broadening.

During the fabrication and the EOF experiments, the thermally grown oxide plays several roles: (1) The growth of the oxide is responsible for the reduction of

the channel dimensions. (2) The oxide on the backside serves as an etch mask during the release process. (3) Depending on the orientation and size, the released channels can be underetched so that they become free-standing. (4) The silicon dioxide provides a transparent electrical isolation, which is appropriate for optical detection and electroosmotic pumping.

High field strength with low voltage can principally be achieved by filling the column with two different concentrations of the same buffer. Unfortunately, field-amplified capillary electrophoresis comes with the peak-broadening mechanism originating from the mismatch of electroosmotic velocities of the two buffer systems. Another approach is presented in this study, where an electroosmotic flow velocity of about 110 $\mu\text{m}/\text{s}$ at an electrical field strength of 277 V/cm in a 280- μm -long nanochannel with an applied potential of 20 V was demonstrated. To assure a plug-flow-like EOF-profile nanochannel cross-section were clearly above the double layer thickness.

A concept to combine the advantages of nanochannels with millimeter-sized reservoirs is presented. By designing the resistances of microfluidic access channel and nanochannels, field strengths up to 600 V/cm typically used in capillary electrophoresis were achieved. The micro- and nanofluidic channels systems were characterized with EOF-measurements. More EOF-studies and

Table 2 Overview of the calculated electroosmotic bulk mobilities μ_b in the micro- and nanofluidic channel systems at different electrical field strengths μ_b and the corresponding standard deviation (SDEV) were calculated from three manually read out measurements of the same type as shown in Fig. 5

Nanochannel length (μm)	μ_b ($\text{cm}^2/\text{V s}$) \pm SDEV @ 5 V	μ_b ($\text{cm}^2/\text{V s}$) \pm SDEV @ 10 V	μ_b ($\text{cm}^2/\text{V s}$) \pm SDEV @ 20 V	μ_b ($\text{cm}^2/\text{V s}$) \pm SDEV @ 40 V
80	$2.02 \times 10^{-4} \pm 8.4 \times 10^{-6}$	$1.65 \times 10^{-4} \pm 2.9 \times 10^{-5}$	$2.07 \times 10^{-4} \pm 2 \times 10^{-5}$	–
280	–	$1.91 \times 10^{-4} \pm 1.1 \times 10^{-5}$	$2.02 \times 10^{-4} \pm 2 \times 10^{-5}$	$1.94 \times 10^{-4} \pm 3.8 \times 10^{-6}$
980	–	–	$3.43 \times 10^{-4} \pm 2.1 \times 10^{-6}$	$3.31 \times 10^{-4} \pm 3.8 \times 10^{-5}$

models with varying channel geometry may elucidate the flow behavior in more such complicated systems.

The number of necessary microfluidic access channels per nanochannel considerably increases for 2D-nanochannels. Obviously new solutions to reduce evaporation effects of microfluidic reservoirs would solve most problems. A future nanofluidic chip must thus include evaporation protected and miniaturized reservoirs as well as micro- and nanofluidic channels.

Acknowledgements This work was financed by the Centre Suisse d'Electronique et Microtechnique (CSEM). Helpful discussions with Dr. H. Heinzlmann and Dr. K. Knop from CSEM are gratefully acknowledged. The authors would like to thank in particular the technical staff of ComLab, the joint IMT-CSEM clean room facility.

References

- Baba M, Sano T et al (2003) DNA size separation using artificially nanostructured matrix. *Appl Phys Lett* 83(7):1468–1470
- Cabodi M, Turner SWP et al (2002) Entropic recoil separation of long DNA molecules. *Anal Chem* 74(20):5169–5174
- Cao H, Tegenfeldt JO et al (2002a) Gradient nanostructures for interfacing microfluidics and nanofluidics. *Appl Phys Lett* 81(16):3058–3060
- Cao H, Yu ZN et al (2002b) Fabrication of 10 nm enclosed nanofluidic channels. *Appl Phys Lett* 81(1):174–176
- Chien RL, Burgi DS (1992) On-column sample concentration using field amplification in Cze. *Anal Chem* 64(8):489A–496A
- Chien RL, Helmer JC (1991) Electroosmotic properties and peak broadening in field-amplified capillary electrophoresis. *Anal Chem* 63(14):1354–1361
- Chou CF, Bakajin O et al (1999) Sorting by diffusion: an asymmetric obstacle course for continuous molecular separation. *Proc Natl Acad Sci USA* 96(24):13762–13765
- Deal BE, Grove AS (1965) General relationship for thermal oxidation of silicon. *J Appl Phys* 36(12):3770–3778
- Eijkel JCT, Bomer J et al (2004) 1-D nanochannels fabricated in polyimide. *Lab Chip* 4(3):161–163
- Foquet MEH, Korfach J et al (2003) Fluorescence correlation spectroscopy and single fluorophore detection in submicrometer closed fluidic capillaries. *Biophys J* 84(2):474A–474A
- Foquet M, Korfach J et al (2004) Focal volume confinement by submicrometer-sized fluidic channels. *Anal Chem* 76(6):1618–1626
- Guo LJ, Cheng X et al (2004) Fabrication of size-controllable nanofluidic channels by nanoimprinting and its application for DNA stretching. *Nano Lett* 4(1):69–73
- Han JY, Craighead HG (2002) Characterization and optimization of an entropic trap for DNA separation. *Anal Chem* 74(2):394–401
- Han J, Turner SW et al (1999) Entropic trapping and escape of long DNA molecules at submicron size constriction. *Phys Rev Lett* 83(8):1688–1691
- Hibara A, Saito T et al (2002) Nanochannels on a fused-silica microchip and liquid properties investigation by time-resolved fluorescence measurements. *Anal Chem* 74(24):6170–6176
- Huang X, Gordon MJ et al (1988) Current-monitoring method for measuring the electroosmotic flow-rate in capillary zone electrophoresis. *Anal Chem* 60(17):1837–1838
- Hug T, Parrat D et al (2003) Fabrication of nanochannels with PDMS, silicon and glass walls and spontaneous filling by capillary forces. *uTAS proceedings* 2004
- Khandurina J, Jacobson SC et al (1999) Microfabricated porous membrane structure for sample concentration and electrophoretic analysis. *Anal Chem* 71(9):1815–1819
- Kuo TC, Cannon DM et al (2003a) Gateable nanofluidic interconnects for multilayered microfluidic separation systems. *Anal Chem* 75(8):1861–1867
- Kuo TC, Cannon DM et al (2003b) Hybrid three-dimensional nanofluidic/microfluidic devices using molecular gates. *Sens Actuator A-Phys* 102(3):223–233
- Lee C, Yang EH et al (2003) A nanochannel fabrication technique without nanolithography. *Nano Lett* 3(10):1339–1340
- Locascio LE, Perso CE et al (1999) Measurement of electroosmotic flow in plastic imprinted microfluid devices and the effect of protein adsorption on flow rate. *J Chromatogr A* 857(1–2):275–284
- O'Brien MJ, Bisong P et al (2003) Fabrication of an integrated nanofluidic chip using interferometric lithography. *J Vac Sci Technol B* 21(6):2941–2945
- Shultz-Lockyear LL, Colyer CL et al (1999) Effects of injector geometry and sample matrix on injection and sample loading in integrated capillary electrophoresis devices. *Electrophoresis* 20(3):529–538
- Tas NR, Mela P et al (2003) Capillarity induced negative pressure of water plugs in nanochannels. *Nano Lett* 3(11):1537–1540
- Tegenfeldt JO, Cao H et al (2004a) Stretching DNA in nanochannels. *Biophys J* 86(1):596A–596A
- Tegenfeldt JO, Prinz C et al (2004b) Micro- and nanofluidics for DNA analysis. *Anal Bioanal Chem* 378(7):1678–1692
- Thormann W, Zhang CX et al (1998) Modeling of the impact of ionic strength on the electroosmotic flow in capillary electrophoresis with uniform and discontinuous buffer systems. *Anal Chem* 70(3):549–562
- Turner SW, Perez AM et al (1998) Monolithic nanofluid sieving structures for DNA manipulation. *J Vac Sci Technol B* 16(6):3835–3840
- Turner SWP, Cabodi M et al (2002) Confinement-induced entropic recoil of single DNA molecules in a nanofluidic structure. *Phys Rev Lett* 88(12):art. no. 128103
- Verdi L, Miotello A et al (1994) Oxide-growth at a si surface. *Thin Solid Films* 241(1–2):383–387
- Xu W, Uchiyama K et al (2001) Fabrication of polyester microchannels and their applications to capillary electrophoresis. *J Chromatogr A* 907(1–2):279–289
- Yu ZN, Chen L et al (2003) Fabrication of nanoscale gratings with reduced line edge roughness using nanoimprint lithography. *J Vac Sci Technol B* 21(5):2089–2092
- Zaumseil J, Meitl MA et al (2003) Three-dimensional and multilayer nanostructures formed by nanotransfer printing. *Nano Lett* 3(9):1223–1227
- Zhang CX, Manz A (2001) Narrow sample channel injectors for capillary electrophoresis on microchips. *Anal Chem* 73(11):2656–2662